Mechanistic Study of a Ru-Xantphos Catalyst for Tandem Alcohol Dehydrogenation and Reductive Aryl-Ether Cleavage

Stephen C. Chmely,[#,†] Seonah Kim,[#,†,‡] Peter N. Ciesielski,[§] Gonzalo Jiménez-Osés,[||] Robert S. Paton,*[,⊥] and Gregg T. Beckham*[,†,‡,⊗]

[†]National Bioenergy Center, [‡]National Advanced Biofuels Consortium, National Renewable Energy Laboratory, and [§]Biosciences Center, Golden, Colorado 80401, United States

[||]Department of Chemistry and Biochemistry, University of California, Los Angeles, 607 Charles E. Young Drive, Los Angeles, California 90095-1569, United States

[⊥]Chemistry Research Laboratory, Department of Chemistry, University of Oxford, Mansfield Road, Oxford OX1 3TA, U.K.

[⊗]Department of Chemical Engineering, Colorado School of Mines, Golden, Colorado 80401, United States

S *Supporting Information*

ABSTRACT: We employ density functional theory (DFT) calculations and kinetics measurements to understand the mechanism of a xantphos-containing molecular ruthenium catalyst acting on an alkyl aryl ether linkage similar to that found in lignin to produce acetophenone and phenol. The most favorable reaction pathway suggested from DFT is compared to kinetics measurements, and good agreement is found between the predicted and the measured activation barriers. The DFT calculations reveal several interesting features, including an unusual 5-membered transition state structure for oxidative insertion in contrast to the typically proposed 3-membered transition state, a preference for an O-bound over a C-bound Ru—enolate, and a significant kinetic preference for the order of product release from the catalyst. The experimental measurements confirm that the reaction proceeds via a free ketone intermediate, but also suggest that the conversion of the intermediate ketone to acetophenone and phenol does not necessarily require ketone dissociation from the catalyst. Overall, this work elucidates the kinetically and thermodynamically preferred reaction pathways for tandem alcohol dehydrogenation and reductive ether bond cleavage by the ruthenium-xantphos catalyst.

KEYWORDS: *Ru-xantphos, aryl-ether cleavage, dehydrogenation, oxidative reduction, lignin deconstruction, reductive elimination*
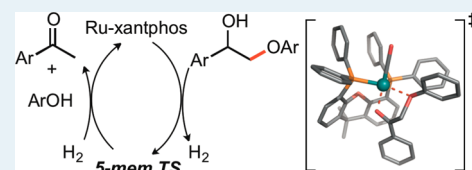
INTRODUCTION

Homogeneous molecular ruthenium species are prized for their ability to perform a number of useful organic transformations via an assortment of remarkable mechanisms, including consecutive catalytic reactions in which the product of a particular reaction is used as the substrate in a second catalytic cycle that uses the same catalytic species.[1,2] In one such example,[3,4] a C—C bond forming reaction between a ketonitrile and an alcohol is catalyzed by a ruthenium complex that is chelated by the bidentate phosphine 4,5-bis-(diphenylphosphino)-9,9-dimethylxanthene (xantphos). This "hydrogen-borrowing" mechanism has been exploited in numerous other reactions involving related ruthenium complexes.[5] The presence of the xantphos ligand is crucial to the dehydrogenation activity of these species, as evidenced by the drop in (or absence of) activity reported by substituting other bidentate phosphine ligands. The ability of these ligands to promote a variety of catalytic transformations is thought to be a consequence of a combination of steric and electronic effects.[6−9]

There are many additional examples of molecular ruthenium catalysts that contain a xantphos ligand, and the reactivity of these compounds is quite varied. Ru-xantphos species promote a catalytic Knoevenagel reaction,[3,4] the conversion of oxide ethers into nitriles,[10] the synthesis of heterocyclic compounds,[11,12] and the hydroformylation of alkenes.[13] In addition, Ru-xantphos has been employed extensively in the oxidation of alcohols: the conversion of 1,4-alkynediols,[14−16] the oxidation of alcohols using levulinic acid as an oxidant,[17] and the conversion of alcohols to methyl esters[18,19] and alkenes[20] have all been reported.

Ruthenium-containing molecular catalysts are also frequently encountered in reactions involving a C—O bond cleavage. A number of transformations have been recently reviewed[21] involving the cleavage of C(sp²)—O bonds. In contrast, to our knowledge there are fewer examples of cleavage of C(sp³)—O bonds. The cleavage of C(sp³)—O bonds is important for the deconstruction and valorization of biomass, where ether bonds are prevalent. To that end, in 2010, Nichols et al. reported the sequential acceptorless dehydrogenation of an alcohol moiety followed by reductive cleavage of a C—O bond in a model glycerolaryl compound by the Ru-xantphos precatalyst RuH₂CO(PPh₃)(xantphos).[22] Wu et al. more recently reported additional details and results on a wider substrate range for the

Scheme 1. Proposed Mechanism for the Catalytic Deconstruction of 1 by [Ru]H$_2$
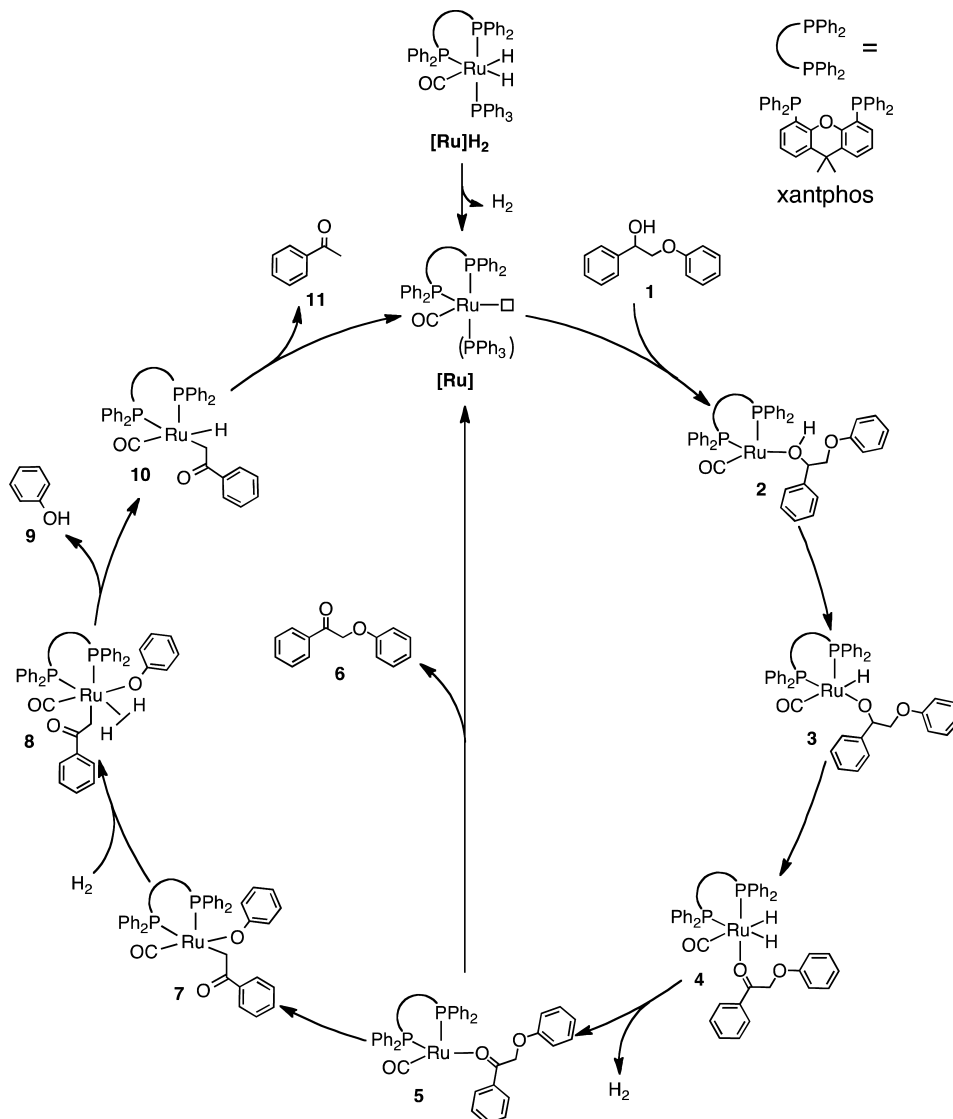
same Ru-xantphos catalyst, and confirmed that the catalytic cycle likely proceeds via a ketone intermediate.[23] Quite recently, vom Stein et al. demonstrated that a Ru(II)-complex with a trimethylenemethane ligand also effects the same transformation on the glycerolaryl compound used by Nichols et al.[24] In the report from Nichols et al., the substrate used in this reaction (2-phenoxy-1-phenylethan-1-ol, 1) is structurally similar to the glycerolaryl ether linkages that are ubiquitous in the naturally occurring heteropolymer lignin, and as such, mechanistic insights to this reaction could be crucial to using lignin as a renewable source of fuels and chemicals. As lignin can comprise up to 30−40% of the plant cell wall depending on the feedstock,[25,26] and, despite many technical challenges regarding its isolation and utilization, there is significant incentive to elucidate new reaction mechanisms for deconstructing lignin for designing biofuel processes.[27,28] While there have been a number of recent reports regarding the selective deconstruction of lignin model compounds using molecular ruthenium,[22] vanadium,[29−31] cobalt,[32−34] titanium,[35] and nickel catalysts,[36,37] there remains much work to be done in this exciting and burgeoning field.

Here, we apply density functional theory (DFT) calculations and experimental kinetics measurements to elucidate the mechanism of the Ru-xantphos-catalyzed reaction of 2-phenoxy-1-phenylethan-1-ol (1) to acetophenone and phenol, first reported by Nichols et al.[22] To begin, we discuss the computational approach used in detail. Next, we discuss the catalytic mechanism of conversion of 1 to 9 and 11 as shown in Scheme 1 above, including the dehydrogenation step to form a ketone intermediate, the C−O bond cleavage step, and the hydrogenation and elimination steps to form the products. Then, we outline the overall set of catalytic cycles suggested from the DFT calculations. We conclude with experimental results regarding the kinetic parameters of the reaction.

■ **RESULTS AND DISCUSSION**

Computational Studies and Mechanistic Elucidation Using DFT. The deconstruction of 2-phenoxy-1-phenylethan-1-ol (1) was modeled with DFT calculations with Gaussian 09[38] using the M06-2X functional of Zhao and Truhlar.[39] M06-2X is a hybrid meta-generalized gradient approximation (meta-GGA) density functional which, through the inclusion of a local spin kinetic energy density term in the exchange-correlation
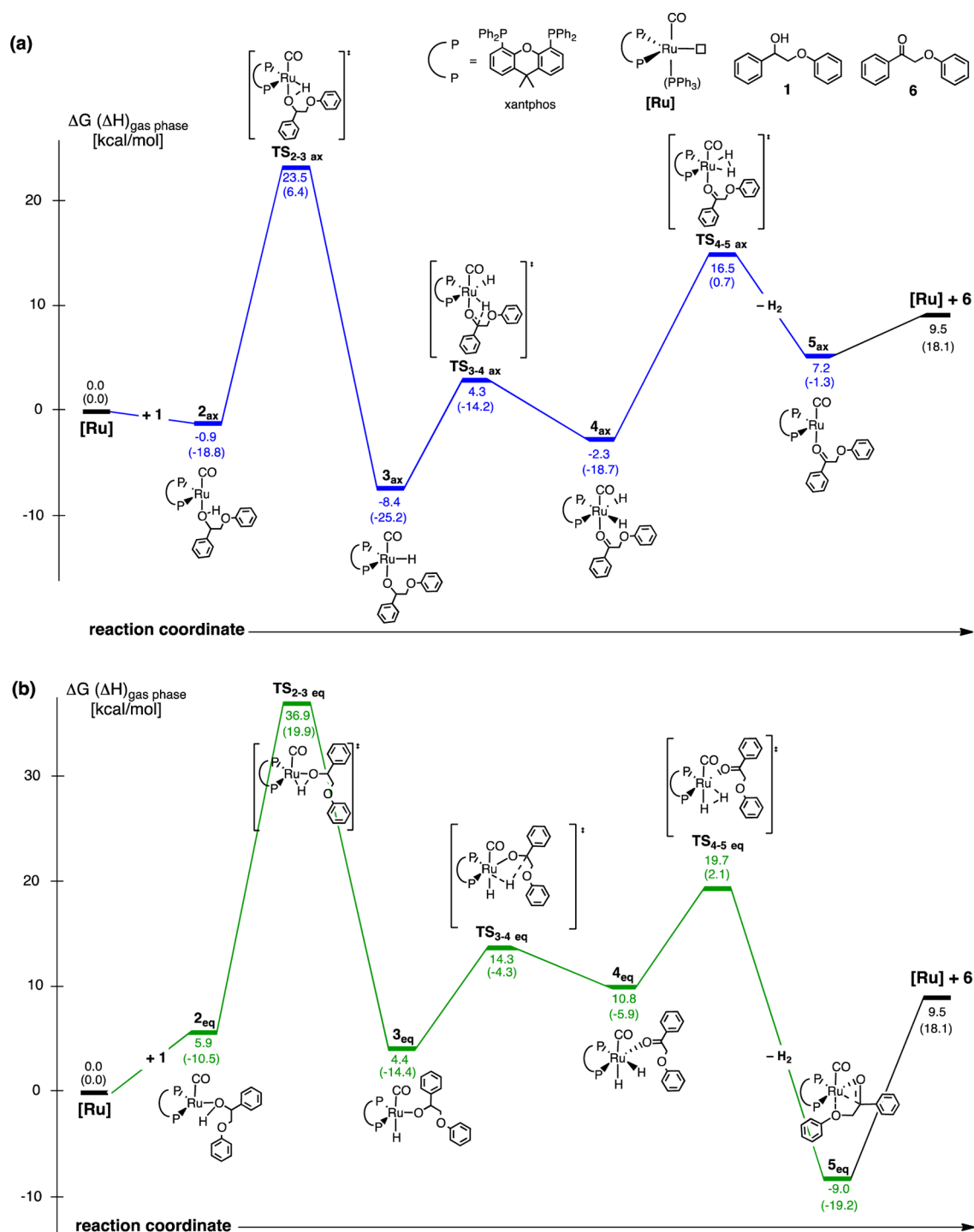
(a)

(b)

Figure 1. Gibbs free energy diagram for the dehydrogenation of **1** to **5**, with the dissociation of **5** to form [**Ru**] and **6** shown as well. Enthalpies for each state are shown in parentheses. (a) Free energy landscape with an axial configuration of the substrate relative to the catalyst. (b) Free energy landscape with an equatorial configuration for the substrate relative to the catalyst.

functional, has been shown to be effective at modeling thermochemical and kinetic parameters, particularly where nonlocal dispersion interactions play a role.[40−44] In reactions involving changes in C−C bonding such as the aldol, Mannich, and α-aminoxylation reactions, Houk and co-workers have shown that M06-2X largely avoids systematic errors in barrier heights and reaction energies of up to 10 kcal/mol present with, for example, B3LYP.[45] Zhao and Truhlar have performed a comprehensive study of the catalytic cycle for Grubbs second-generation Ru-catalyzed olefin metathesis, finding that the

M06-2X and M06 functionals were among the best tested: averaging over the entire catalytic cycle M06-2X and M06 give mean unsigned errors relative to CCSD(T) of 4.1 and 1.2 kcal/mol, respectively, while the error for the widely used B3LYP functional was 11.0 kcal/mol.[46] Below, we report energetics computed with M06-2X. However, the M06 functional (in which the percentage of Hartree−Fock exchange is halved in relation to M06-2X) gives very similar results for the catalytic cycles examined here as described in the Supporting Information, Figures S1 and S2. In addition, the optimized

geometry of catalyst $[\text{Ru}]\text{H}_2$ with M06-2X shows good agreement with the X-ray crystallographic values[4] of key Ru−P and Ru−C distances as shown in Supporting Information, Figure S3. All subsequent optimizations were performed at the M06-2X/6-31G(d) level of theory, also using the LANL2DZ double-ζ valence basis set and associated effective core potential (ECP) to describe Ru.[47] Single point energies were computed on all optimized geometries with the larger 6-311++G(d,p) and LANL2DZ basis sets.[48] A fine grid density was used for numerical integration in all DFT calculations. Harmonic vibrational frequencies were computed for all optimized structures to verify that they were either minima or transition structures, possessing zero imaginary frequencies or one imaginary frequency, respectively. Each transition state was further calculated by intrinsic reaction coordinate (IRC) calculations to confirm that such structures indeed connect two relevant minima.[49−53] We attempted to locate the lowest energy transition structure by optimizing from different starting geometries; we tested all possible configurations by changing the O−C−C−O dihedral angle of each substrate. Low energy configurations are reported. Free energies were evaluated at 298 K including zero point vibrational energies. All structures are depicted with CYLview.[54] Effects on computed geometries and energetics of the catalytic cycle were evaluated with single point energies in a conductor-like polarizable continuum model[55,56] (CPCM) of xylene solvation, which is the solvent used in the kinetics experiments. The energies of intermediates and transition structures closely match the gas phase results, and the overall energetic span of the catalytic cycle is reduced by 2.4 kcal/mol from the gas phase value. As such, below we report only gas-phase calculations for the investigated steps in the catalytic cycle. For all cases, free energies and enthalpies are reported in kcal/mol, and were calculated with M06-2X/6-311++G(d,p)//M06-2X/6-31G(d) with LANL2DZ for Ru. Unless otherwise stated, figures in the text quote free energies and enthalpies computed at this level of theory.

In the studies from Nichols et al.[22] and Wu et al.,[23] the authors propose a catalytic mechanism for Ru-xantphos action on aryl-ether linkages. Here, we have expanded upon their proposed mechanisms to incorporate the full suite of hypothesized elementary steps, as shown in Scheme 1. Scheme 1 expands on the original mechanistic proposal for the catalytic dehydrogenation of **1** to **5**,[4] the C−O bond cleavage and reductive elimination steps from **5** to **9** and **11**, and the order of product release in the C−O bond cleavage steps, which are reversed from the original proposal.[22] As will be discussed below, the steps presented in Scheme 1 represent the preferred elementary steps, based on the DFT calculations. We also compare alternative mechanisms for several components of the overall cycle.

Scheme 1 begins with the loss of H_2 to form $[\text{Ru}]$, which contains a labile PPh_3 that can be lost during the reaction, as reported previously.[4] This (CO)Ru(xantphos) molecule was proposed to be the catalytically active species by Wu et al. in the hydrogenolysis of lignin model compounds.[23] An incoming substrate molecule **1** coordinates to $[\text{Ru}]$ to form **2**. Oxidative addition of $[\text{Ru}]$ across the O−H bond of **1** proceeds through $\text{TS}_{2−3}$ to form **3**, which is followed by a β-hydride elimination that proceeds through $\text{TS}_{3−4}$ to generate **4**. The reductive elimination of H_2 leads to **5**. Molecule **5** can dissociate to form **6** and $[\text{Ru}]$, or proceed through $\text{TS}_{5−7}$ to form enolate **7** via a C−O bond cleavage. $\text{TS}_{5−7}$ is the key step in which the lignin model fragment is deconstructed. A molecule of H_2 can then

associate to **7** to form **8**, which contains a side-on-bound H_2 moiety. Release of phenol (**9**) occurs via $\text{TS}_{8−10}$ to form **10**, which is followed by release of acetophenone (**11**) and regeneration of $[\text{Ru}]$ to restart the catalytic cycle. We discuss the catalytic dehydrogenation, C−O bond cleavage, reductive elimination, and product release portions of the catalytic cycle separately below.

For each case discussed, we examined the configuration of the substrates to the catalyst. We assigned the equatorial plane of the catalyst as containing the two phosphine groups of the xantphos ligand, and focused on substrate binding in an axial fashion (i.e., *trans* to one of the −PPh$_2$ groups) as illustrated in the Supporting Information, Figure S4. These stereoisomers were optimized for all intermediates and transition states along the entire catalytic cycle, as described below.

Catalytic Dehydrogenation Reaction Pathway. Using DFT, we examined both an axial and an equatorial bound substrate, starting with **2**. We were interested in elucidating the kinetic *trans* effect imparted by CO or xantphos using DFT by alternating substrate coordination in the axial or equatorial positions, respectively. The free energy profiles for the dehydrogenation of **1** to form **5** are shown in Figure 1a and 1b for the axial and equatorial cases, respectively.

Figure 1a shows the free energy landscape from DFT calculations for axial coordination of **1** to $[\text{Ru}]$, which is thermoneutral (exergonic by 0.9 kcal/mol). Oxidative addition of $[\text{Ru}]$ across the O−H bond proceeds through $\text{TS}_{2−3\text{ ax}}$ to form 3_{ax}; the free energy of activation for this process is 24.4 kcal/mol. Subsequent β-hydride elimination to form a ruthenium dihydride with a coordinated molecule of **6** (complex 4_{ax}) is endergonic by 6.1 kcal/mol, and the activation barrier for this process, which proceeds through $\text{TS}_{3−4\text{ ax}}$, is 12.7 kcal/mol. Reductive elimination of H_2 gas and formation of complex 5_{ax} is also endergonic (9.5 kcal/mol) and proceeds through $\text{TS}_{4−5\text{ ax}}$ with a free energy of activation of 18.8 kcal/mol. Dissociation of the substrate molecule **6** has no kinetic barrier and is essentially reversible (endergonic by 2.3 kcal/mol).

Figure 1b shows the free energy landscape from DFT calculations for equatorial coordination of **1** to $[\text{Ru}]$. While this coordination is reversible when **1** is coordinated axially, coordination of **1** in an equatorial position is an endergonic process (ΔG = 5.9 kcal/mol). The activation barrier for oxidative addition of $[\text{Ru}]$ across the O−H bond has a free energy of activation of 31.0 kcal/mol, which is 6.6 kcal/mol higher in free energy than the related step using an axial-bound substrate. We hypothesize that this is due to the enhanced reaction rate imparted by the configuration of the molecule whereby the CO ligand is located *trans* to the substrate ligand. Calculated transition structures such as $\text{TS}_{2−3\text{ eq}}$, where electron density is *increasing* at the metal center, are energetically stabilized when a portion of that electron density is *trans* to a ligand that can accept electron density into ligand antibonding orbitals with π-pseudosymmetry such as CO.[57] This effect is also apparent with phosphine ligands, although it is attenuated by donation of lone-pair electron density from the P-atom to the metal center.[58] A comparison of the calculated structures of 2_{eq} and $\text{TS}_{2−3\text{ eq}}$ shows an increase in the Ru−CO distance (1.832 to 1.951 Å), a decrease in the C−O$_{\text{carbonyl}}$ distance (1.160 to 1.153 Å), and an increase in the C−O$_{\text{carbonyl}}$ stretching frequency (2057 to 2080 cm^{-1}) from 2_{eq} to $\text{TS}_{2−3\text{ eq}}$, respectively. This is indicative of a stabilizing "push-pull" interaction between donor alkoxy and acceptor CO ligand
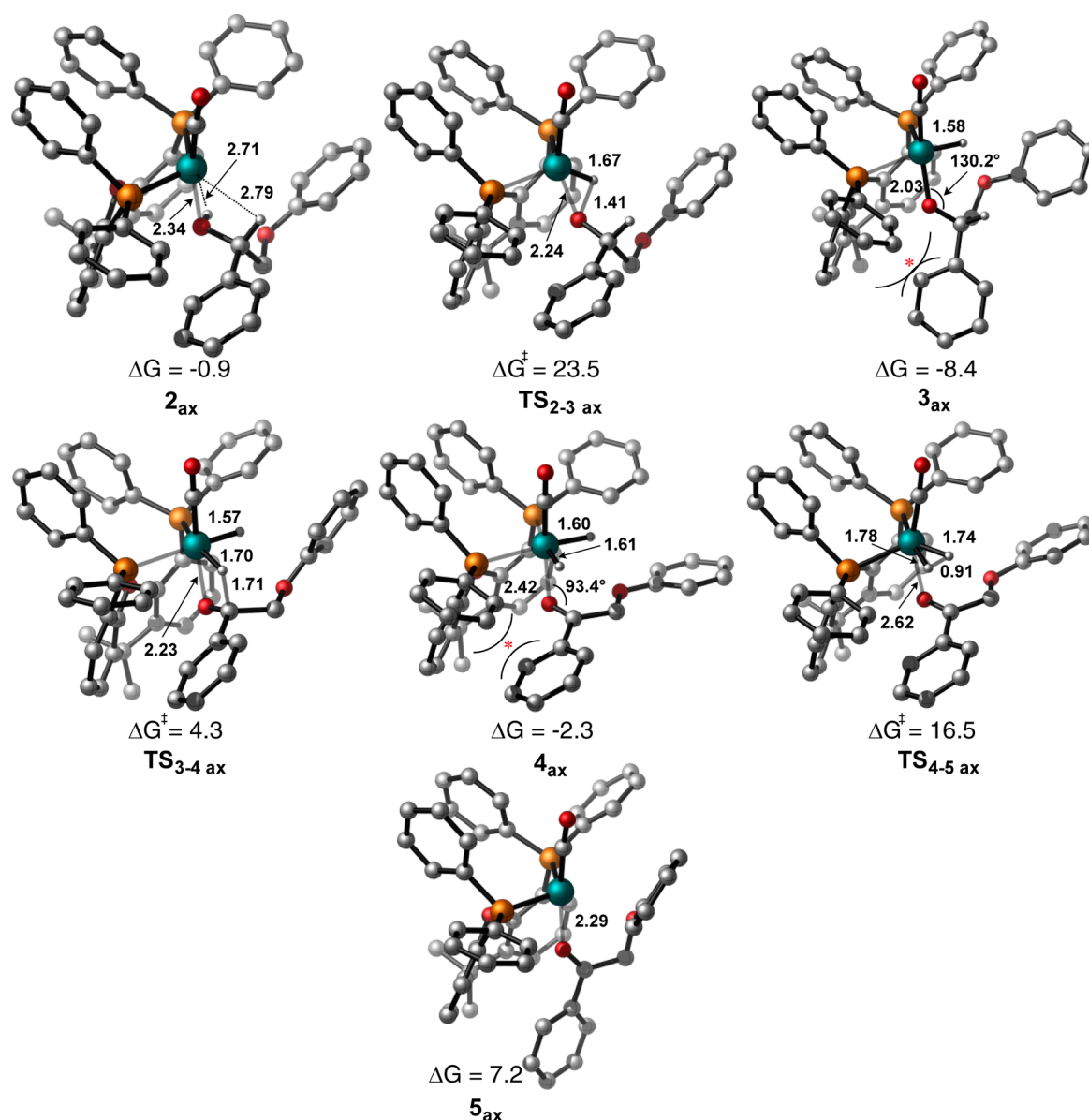
Figure 2. M06-2X/6-31G(d) (LANL2DZ for Ru) optimized structures of intermediates and transition structures for dehydrogenation of **1** in the axial binding configuration with selected hydrogen atoms omitted for clarity and selected bond distances in Å. Free energies are given in kcal/mol.

present when the substrate is axially bound.[59−63] Because the free energy of activation of $TS_{2−3}$ is lower when **1** is bound axially ($TS_{2−3\ ax}$), we propose that this is the preferred substrate coordination mode (i.e., when **1** is *trans* to CO).

The optimized geometries of $2_{ax}−5_{ax}$ for the preferred axial configurations and the related $TS_{2−3\ ax}−TS_{4−5\ ax}$ are shown in Figure 2. Complex 2_{ax} contains an axial CO ligand and the xantphos moiety is arranged in an equatorial fashion about the Ru center, with the phenyl groups of the phosphine arms oriented in the same direction as the CO ligand and the xantphos backbone oriented in the opposite direction. This allows for coordination of the substrate molecule **1** in an axial site that is *trans* to CO (∠OC−Ru−O-H = 167.3°). In this arrangement, the Ru center is in close proximity to both the protic hydrogen attached to the O-atom for oxidative insertion as well as the hydridic hydrogen attached to the α-C-atom for subsequent β-hydride elimination. $TS_{2−3\ ax}$ depicts the oxidative insertion of the Ru fragment across the O−H bond. Here, the O-atom moves closer to the Ru center as the protic hydrogen is

abstracted and also moves closer. In complex 3_{ax}, the alkoxide and hydride moieties are bound to the Ru(II) center.

$TS_{3−4\ ax}$ depicts the transition geometry for the β-hydride extraction. In this step, a 4-membered transition state containing Ru, the alkoxide-O, the C_α, and the related hydride is formed, where the hydride is essentially equidistant from the Ru and C_α. The Ru−H distances of 1.60 and 1.61 Å in complex 4_{ax} agree well with the related Ru−H distances in the crystal structure of $[Ru]H_2$ (1.60 and 1.69 Å).[4]

The TS geometry for the reductive elimination of H_2 gas ($TS_{4−5\ ax}$) shows a lengthening of the Ru−H distances and a contraction of the H−H distance. The Ru−H bond of $TS_{4−5\ ax}$ (1.74 Å) is slightly elongated compared to the dihydride complex, 4_{ax} (1.60 and 1.61 Å, respectively). The H−H distance of $TS_{4−5\ ax}$ of 0.91 Å belongs to the category of "true H_2 complexes" by the definition of Kubas et al.[64] There is a slight movement of the ketone substrate away from the Ru center, which is accompanied by a slight twist of this ligand to bring the face of the B-ring of the substrate closer to the Ru
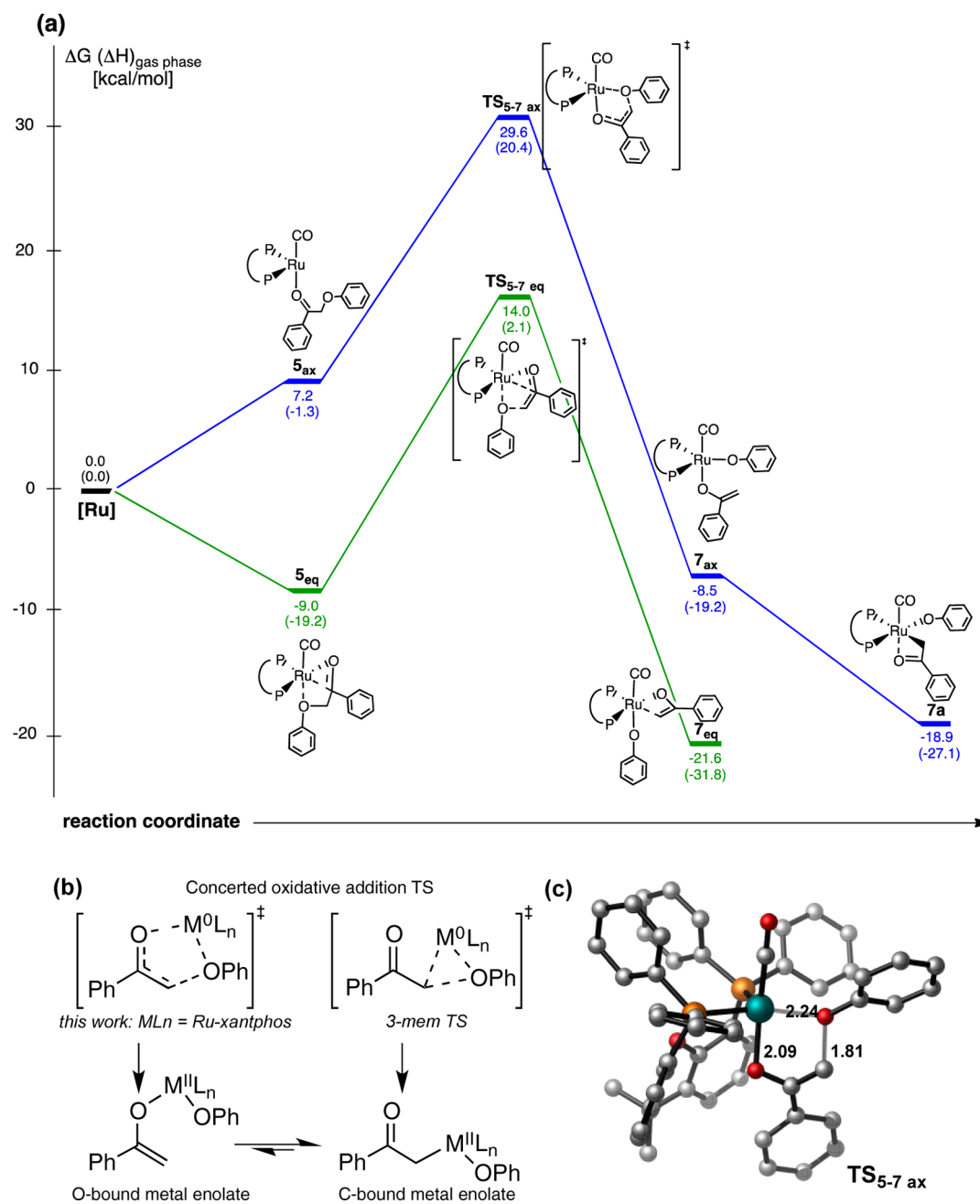
(a)

(b) Concerted oxidative addition TS

(c)

Figure 3. Possible mechanisms considered for the C−O insertion reaction of **5**. (a) Pathways for concerted oxidative addition of Ru across the C−O bond shown in both an axial (blue) and equatorial (green) configuration for the substrate, **5**. For all cases, free energies and enthalpies (parentheses) are reported in kcal/mol. (b) Potential transition structures for C−O activation leading to O- and C-bound M−enolates. Optimized structures of the O-bound **TS$_{5-7 \, ax}$** (5 membered TS). Hydrogen atoms omitted for clarity. Bond distances are given in Å.

center. Elimination of H_2 results in the formation of **5$_{ax}$**, which contains a Ru−O bond of 2.29 Å. The formal oxidation state of the metal changes from Ru(II) to Ru(0). Complex **5$_{ax}$** is apparently a thermodynamically stable 16e^- complex with a disphenoidal "see-saw" geometry. There do not appear to be any additional agostic interactions between the Ru center and any proximal C−H bonds. Generation of highly reactive, unsaturated intermediates such as **5$_{ax}$** has been previously proposed as an explanation for the exceptional reactivity of Ru-hydride catalyst species in the dehydrogenation and decarbonylation of alcohols.[65] Overall, the catalytic dehydrogenation of **1** (i.e, [**Ru**] + **1** → [**Ru**] + **6** + H_2) is somewhat endergonic (9.5 kcal/mol), which is in good agreement with experimental

evidence that shows that the acceptorless dehydrogenation of alcohols are typically endergonic processes which are driven to completion by a tandem exergonic process.[66]

Mechanism of Catalytic C−O Bond Cleavage. Following dehydrogenation of the alcohol substrate **1**, the catalyst promotes a reductive cleavage of the α-aryloxy C−O bond using the H_2 formed previously. DFT calculations were performed to investigate the fate of complex **5** to establish the likely mechanism of the subsequent steps to form acetophenone and phenol products. Notably, oxidative addition of the Ru catalyst into the C_α−O bond was found to occur via a novel concerted 5-membered transition structure, which neither resembles the concerted 3-membered nor the stepwise
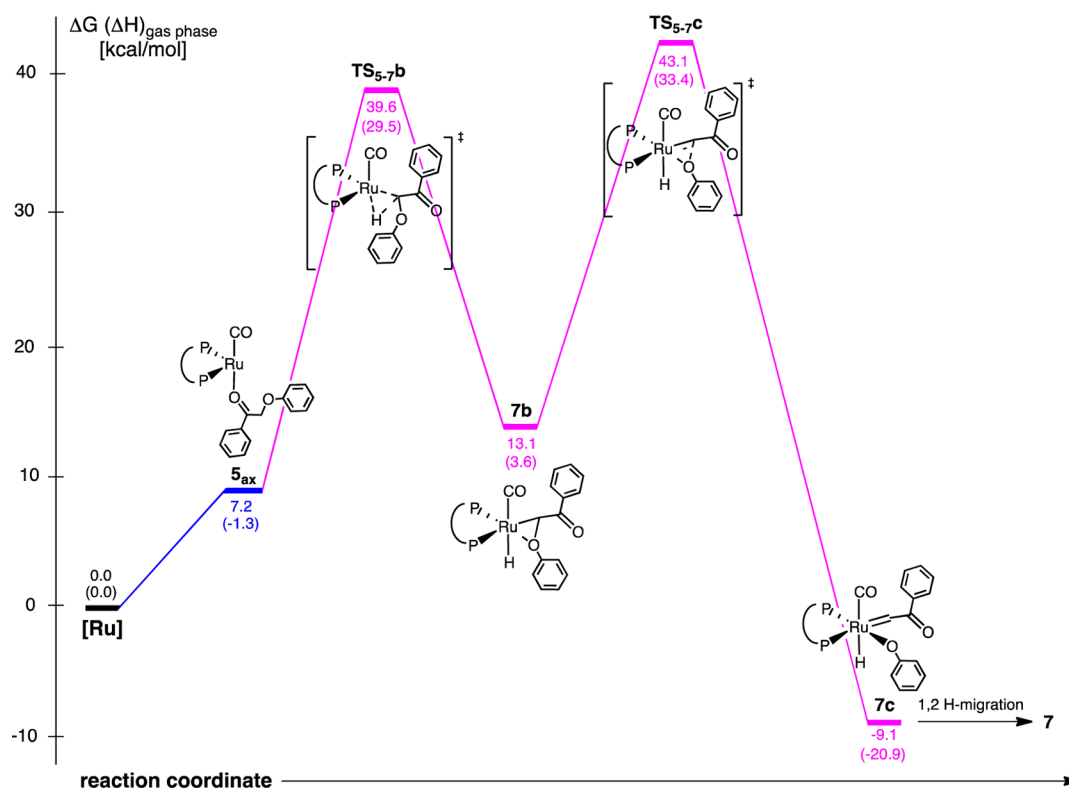
Figure 4. Pathway for C−H oxidative insertion, Ru-alkylidene formation, and hydrogen migration.

S_N2 transition structure usually found for oxidative insertions of metal catalysts into C−X bonds.[67] The extent of C−O bond distortion in this TS is significantly less than for the analogous 3-membered oxidative insertion and is thus kinetically preferred over the possible alternative reaction pathways that could potentially occur instead. The preferred mechanism for the C−O activation pathway, which proceeds via a 5-membered transition structure, is presented in Figure 3.

We were able to successfully locate two transition structures corresponding to the concerted oxidative insertion of the catalyst into the C−O bond, $TS_{5−7}$, differing in the axial or equatorial positioning of the substrate with respect to the catalyst. The free energy of activation for this step is 22.4 kcal/mol for the axial case ($TS_{5−7\ ax}$) and 23.0 kcal/mol for the equatorial case ($TS_{5−7\ eq}$) from the respective bound substrate configurations. As mentioned above, the geometry of $TS_{5−7}$ is unusual since the insertion takes place via a five-membered cyclic transition structure. In contrast, the oxidative insertion of transition metal catalysts via either concerted three-centered transition structures or a stepwise S_N2-recombination process have been explored extensively with DFT calculations.[67] Rather, in $TS_{5−7\ ax}$ the metal is coordinated to both oxygen atoms forming a five-membered cyclic structure, as shown in Figure 3. This transition structure leads directly (following the IRC) to the oxygen bound Ru−enolate shown in Figure 3. We posit that this type of geometry for an oxidative insertion transition structure will be accessible (and possibly energetically preferable) wherever the C−X bond is vicinal to a carbonyl or functional group equivalent (e.g., imine). We also optimized the structure of a C-bound enolate, **7a**, which is 10.4 kcal/mol more stable. This is the expected product from a conventional 3-membered oxidative insertion into the C−O bond, although here such a transition structure could not be located. Instead, the O-bound enolate is formed first, which may then be able to

interconvert to the more stable C-bound form. Interconversion between isomeric enolates could occur via an η^3-bound intermediate, although attempts to optimize this putative transition structure were unsuccessful. Anderson and Bergman have previously characterized (by ^{1}H, ^{13}C, and ^{31}P NMR spectroscopy) both C- and O-bound acetone Ru-enolates, and shown equilibration to occur over a wide temperature range of 5−60 °C.[68,69] More recently in the aldol additions of Ru-enolates to aldehydes, the C-bound Ru(II)−enolate form was observed spectroscopically but found to be catalytically inactive, suggesting this intermediate is a catalyst resting state while the O-bound form is necessary for the reaction to progress.[70] Our computational findings support this idea: we computed the subsequent reductive elimination steps proceeding via C- and O-bound enolate forms, finding the O-bound enolate to be more reactive toward these steps, as shown in Supporting Information, Figure S5.

Observations of Catalyst Selectivity. In addition to the experimentally observed C−O activation pathway,[22] we also investigated the potential competing mechanism via an initial C−H oxidative insertion step (rather than C−O oxidative insertion) from 5_{ax}, as shown in Figure 4. Aryl ethers have been observed to react with $RuH_2CO(PPh_3)_3$, undergoing kinetically favored aryl C−H insertion, while C−O insertion was thermodynamically preferred.[71] In addition, $Ru(H)_2(CO)$-$(PR_3)_3$ has been shown to catalyze the addition of the ortho-C−H bond of benzaldehyde to ethylene.[72] To understand the successful C−O reductive cleavage in 5_{ax}, it is thus important to characterize competing pathways. The sequence of steps in which oxidative C−H addition is followed by α-aryloxy elimination to give the Ru−alkylidene **7c** were considered. A subsequent 1,2-migration of a hydride from Ru to the carbene gives the O-bound product **7b**. Both the C−H bond addition $TS_{5−7}$**b** and the C−O bond cleavage $TS_{5−7}$**c** (a three-
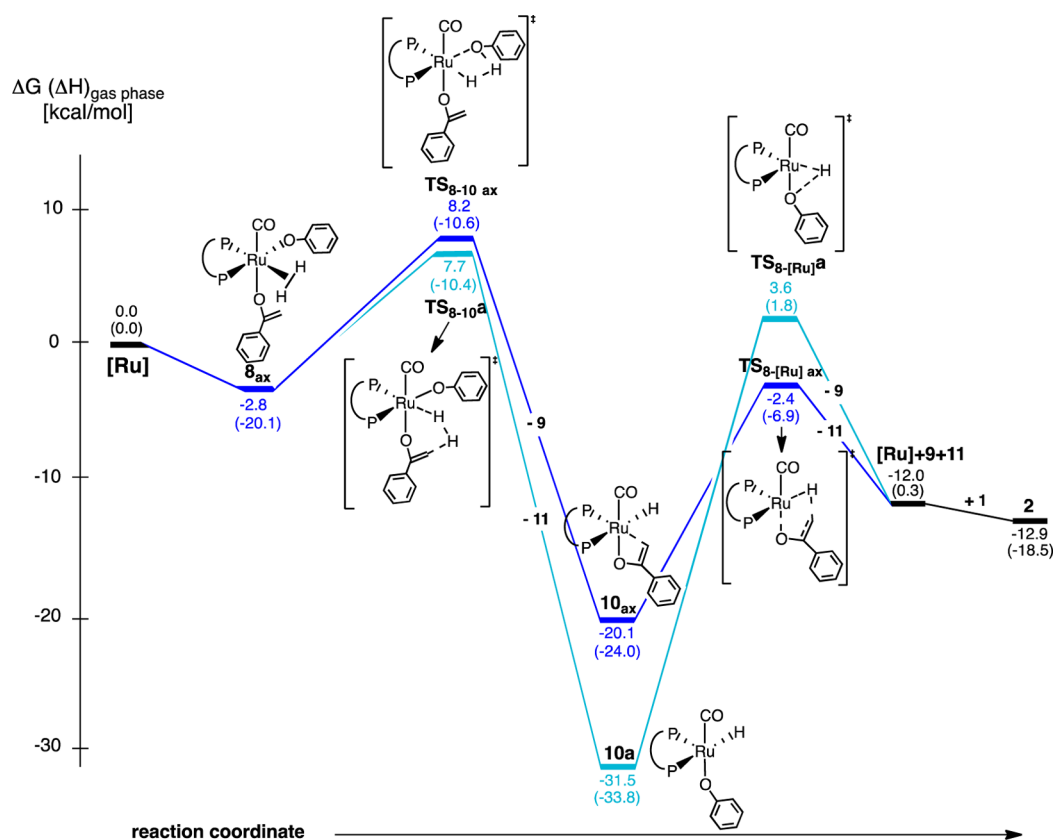
Figure 5. Gibbs free energy (and enthalpy) diagram for hydrogenation and reductive elimination steps (blue and cyan represent phenol or acetophenone release first, respectively). Enthalpies for each state are shown in parentheses.
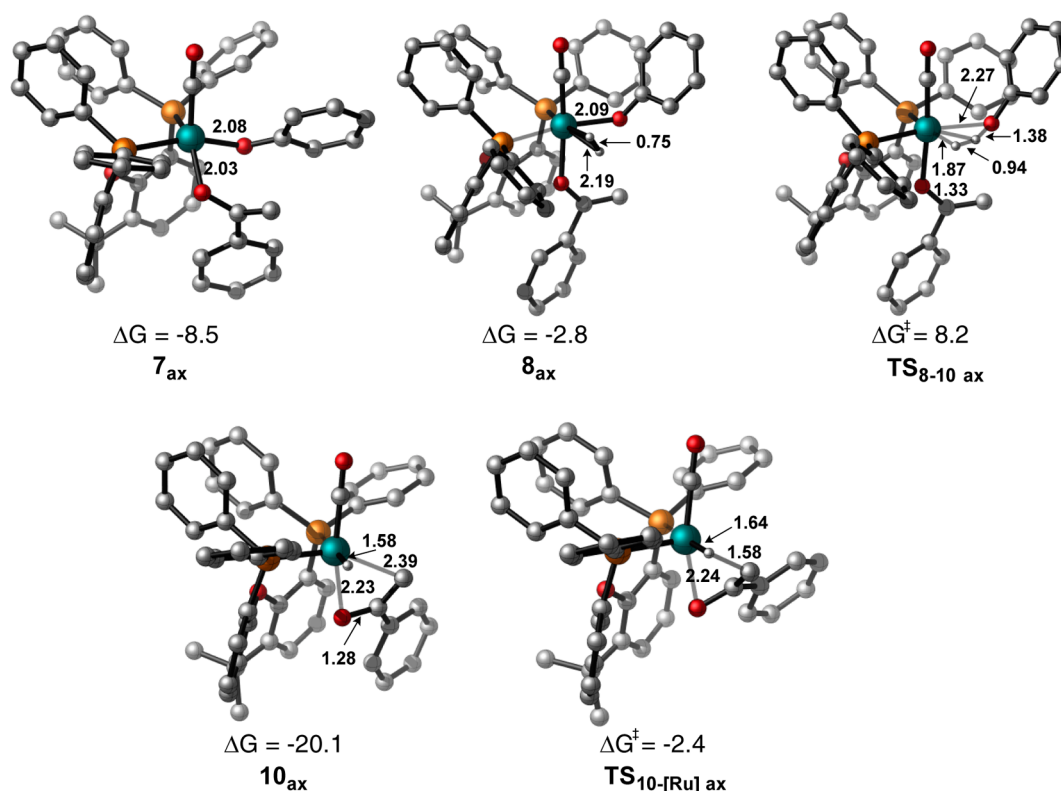

Figure 6. M062X/6-31G(d) (LANL2DZ for Ru) optimized intermediates and transition structures for the C−O bond hydrogenolysis of **6**. Selected hydrogens have been omitted for clarity. Bond distances are given in Å. Energies are given in kcal/mol calculated with M06-2X/6-311++G(d,p)// M06-2X/6-31G(d) with LANL2DZ for Ru.
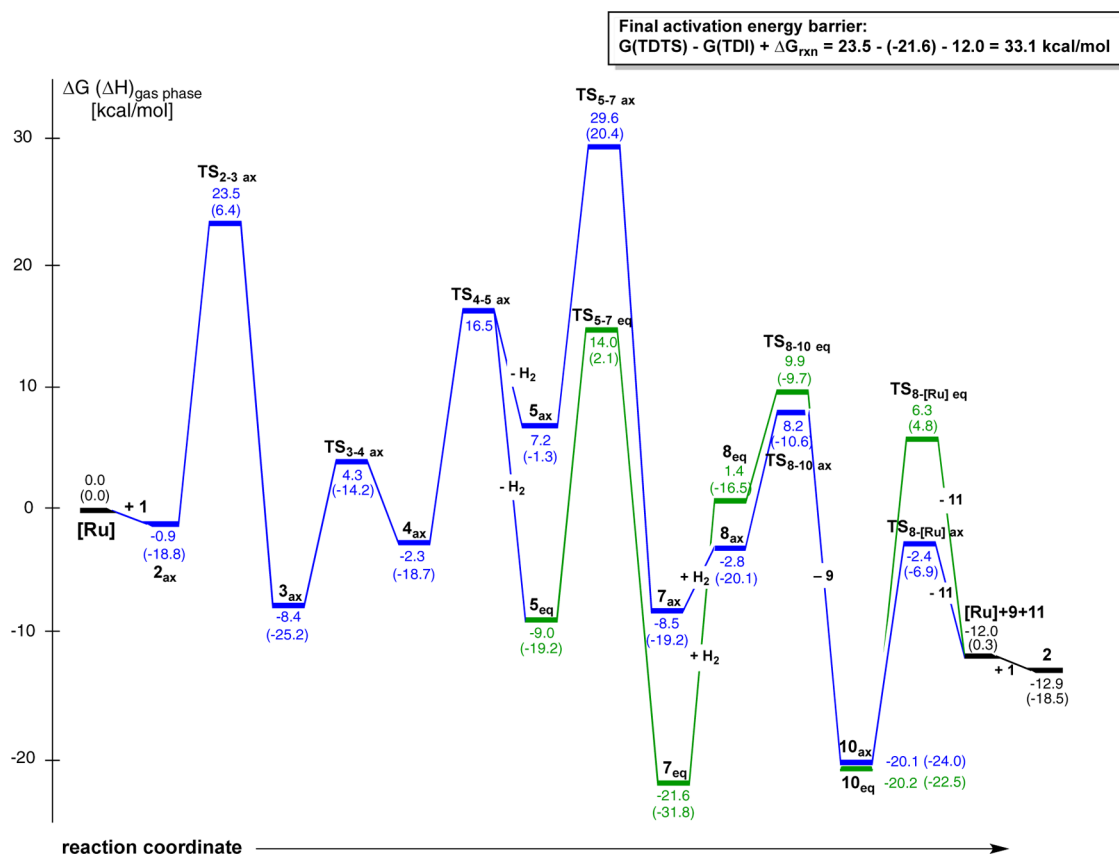
Figure 7. Free energy diagram for the entire catalytic cycle for the axial (blue) and equatorial (green) isomers. The final activation energy barrier is shown in a shadowed box based on the preferred pathway. Enthalpies for each state are shown in parentheses.

membered transition structure) show much higher activation barriers (39.6 and 43.1 kcal/mol, respectively) than the concerted C−O insertion pathway ($TS_{5-7\ ax}$, 29.6 kcal/mol). Thus the observed selectivity for C−O activation results from a pronounced kinetic preference over the C−H activation pathway. Additionally, we computed the activation barrier for the oxidative insertion of Ru into the $C(sp^2)$−O bond, since activation of phenyl ether C−O bonds has been observed experimentally.[73] With a computed barrier of 39.6 kcal/mol, the 3-membered transition structure for this process is much higher in free energy than $C(sp^3)$−O insertion and hence is highly kinetically disfavored. Therefore we conclude that the observed $C(sp^3)$−O activation results from a kinetic preference over competing C−H insertion; this preference is due to the relative stability of $TS_{5-7\ ax}$, which maintains strong Ru−O contacts via a five-membered cyclic structure. Given a strong $C(sp^3)$−O bond must be broken (the homolytic bond dissociation energy in the parent alcohol **1** is ca. 70 kcal/mol at the CBS-QB3 level),[74] the five-membered transition structure minimizes lengthening of the breaking C−O bond relative to the three-membered structure.

Hydrogenation and Reductive Elimination to Form Phenol and Acetophenone. Lastly, we investigated the steps to hydrogenate the acetophenone and phenol precursors after C−O bond cleavage. The results are presented for the O-bound enolate 8_{ax}, which immediately results from the prior oxidative insertion step and coordination of H_2. While the C-bound enolate is more stable, the ensuing barriers for reduction to form the two products were also higher (Supporting

Information, Figure S5), and so we focus our attention on the more reactive intermediate 8_{ax}.

While the order of product release was originally proposed to occur via the successive reductive eliminations of acetophenone (**11**) followed by phenol (**9**), we considered the feasibility of both orders of product release. Figure 5 shows the DFT computed reaction coordinate for this sequence of steps in the catalytic cycle for both possibilities. The first reductive elimination occurs through a σ-bond metathesis type transition structure, in which dihydrogen adds across either Ru−ligand bond. These barriers show little preference for the release of either phenol or acetophenone first. However, the subsequent reductive elimination step is much more facile for release of acetophenone (with an activation barriers of 22.5 kcal/mol vs 35.1 kcal/mol for the release of phenol in this step). Thus, our calculations suggest that the successive release of phenol followed by acetophenone is instead the favored pathway. Wu et al. also recently reported experimental findings that support this order of product release.[23]

The optimized geometries of 7_{ax}, 8_{ax}, and 10_{ax} as well as the related $TS_{8-[Ru]\ ax}$ and $TS_{10-[Ru]\ ax}$ are shown in Figure 6. Complex 7_{ax} contains a phenoxide and an O-bound enolate, and coordination of a molecule of H_2 in a side-on fashion yields 8_{ax}, in which the O-bound enolate is *trans* to the CO ligand and the H_2 ligand and phenol are arranged *trans* to the bisphosphine via an η^2-H_2 complex. The two hydrogen atoms that coordinate after insertion of molecular H_2 interact at an H−H distance of 0.75 Å, which is close to isolated H_2 (0.74 Å).[64] From 8_{ax}, the release of phenol proceeds through $TS_{8-10\ ax}$, whereby the heretofore symmetrically η^2-bound H_2

ligand rotates inward toward the Ru center while the phenoxide ligand moves away from Ru. This arrangement allows for the release of **9** and the formation of **10**$_{ax}$, which contains a π-bound enolate ligand. The final reductive elimination of acetophenone (**11**) occurs via **TS**$_{8\text{-[Ru] ax}}$, which contains a 5-membered transition state consisting of a Ru metallacycle. Subsequently, the catalytic species [**Ru**] is regenerated and the catalytic cycle can restart. Overall, the C–O bond cleavage of **1** is exergonic by 12 kcal/mol.

Overall Reaction Pathway. As discussed above, we considered the stereochemistry at the Ru center throughout the entire cycle. Figure 1 suggests that the dehydrogenation step will occur through axially coordinated species to form **5**$_{ax}$ from **1** and [**Ru**]. Figure 7 shows the free energy landscape for the entire reaction cycle with the substrates in the axial isomer from **1** to **5**$_{ax}$, and both the axial and the equatorial coordination pathways for the C–O bond cleavage step. Murdoch has described a manner for determining the rate-limiting step for a multistep reaction,[75] and Kozuch and Shaik subsequently introduced convenient terminology to describe the relevant rate-determining transition states of a multistep reaction, dubbed the energetic span model.[76] Since a given catalytic cycle occurs a number of times, the apparent activation energy of the reaction depends on the largest energetic gap between any given transition state and any given intermediate, regardless of which occurs first. As a result, the energetic span model can be applied to determine the apparent free energy of activation based on the so-called turnover-frequency-(TOF)-determining transition structure (TDTS) and the TOF-determining intermediate (TDI). For the case where the entire cycle goes from **1** to **9** and **11** via the axial coordination, the activation energy term which limits the TOF of the catalyst uses **TS**$_{5–7\text{ ax}}$ and **3**$_{ax}$, in which case $\Delta G(\text{TDTS}) - \Delta G(\text{TDI}) = 29.6 - (-8.4) = 38$ kcal/mol. If we assume the axial-to-equatorial isomerization of **5** to be rapid or if we assume that **5** can dissociate to **6** easily (as shown in Figure 1), then these two mechanisms can be mixed.[77] The axial and equatorial isomers can interconvert at complex **5**, since the axial isomer has a lower energy barrier for the dehydrogenation step (from complex **2**$_{ax}$ to **TS**$_{4–5\text{ ax}}$), while the equatorial isomer has a lower energy barrier in subsequent C–O bond cleavage steps (from complex **5**$_{eq}$ to **TS**$_{8\text{-[Ru] eq}}$) as shown in Figure 7. Therefore, the TDI (**TS**$_{2–3\text{ ax}}$ from the axial isomer, shown in blue) and the TDTS (**7**$_{eq}$ from the equatorial isomer, shown in green) correspond to the most stable intermediate and transition structure along the reaction coordinate based on the Curtin–Hammett principle.[78] As a result, the final rate-limiting activation energy barrier is $G(\text{TDTS}) - G(\text{TDI}) + \Delta G_{rxn} = 23.5 - (-21.6) - 12.0 = 33.1$ kcal/mol from the preferred axial to equatorial pathway.

Experimental Kinetics of Model Dimer Conversion. The mechanism elucidated by DFT calculations as summarized in Figure 7 involves a Ru-catalyzed C–O bond reduction of **1** to yield monomeric products of acetophenone and phenol through a key intermediate **5**. To identify putative intermediates in their previous study, Nichols et al. showed that **6** can undergo reductive C–O cleavage to yield **9** and **11**, suggesting that the ketone species **6** is a key intermediate.[22] Additionally, the DFT calculations suggest two primary pathways for the reaction of **1** to **9** and **11**: one in which C–O bond cleavage is direct from **1** to **9** and **11** without the dissociation of **5**, and one in which compound **5** dissociates to form **6** and [**Ru**], and, as such, both mechanisms were

considered in the comparison of the theoretical predictions to the experimental measurements.

We monitored the change in concentration with respect to time at 130 °C of starting material **1**, product **9**, and the key intermediate **6** with GC/MS. Because the reaction shown in Scheme 1 evolves H_2, which is later used up as a stoichiometric reactant, we required a reactor system that could contain H_2. We found Teflon-stoppered screw-cap glass reactor tubes ideal for this application. Unfortunately, the use of such reactors precludes the ability to sample the reaction directly for GC/MS analysis during the course of each reaction, as any small loss of H_2 gas during the sampling process would necessarily prevent the reaction from proceeding to completion. As such, we devised a scheme that involved making a stock reaction solution at room temperature, separating it among a number of reactor tubes, and running each reaction in parallel at temperature. Then, we could quench each reaction at a specified time point and collect concentration data for that time point using GC/MS. This method proved effective for gathering concentration data as a function of time, and the average of four experimental measurements is shown in Figure 8 (solid markers). Additional
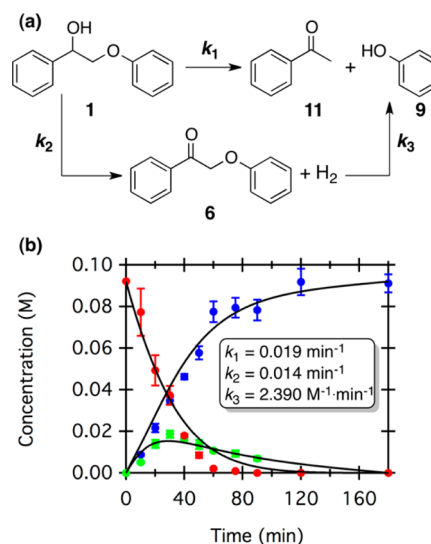

Figure 8. (b) Plot of concentration of **1**, **6**, and **9** (red, green, and blue, respectively) as a function of time for the reaction given by (a). Reaction conditions: [**1**]$_0$ = 0.10 M. The solid lines are the kinetic fits using COPASI. The rate constants for the reaction are shown in the inset. Each data point represents the average of 4 independent measurements.

experimental details are provided in the Supporting Information. We then used COPASI[79] to conduct kinetic simulations to fit these experimental data to various mass action kinetic models, and those fits are shown with the experimental data in Figure 8 with the elementary rate constants, k_1, k_2, and k_3 shown in the inset. We found that a mass action kinetic model that employs a direct conversion of **1** to **9** and **11** and an explicit treatment of the dissociation step to form **6** with first order kinetics for each species best models the experimental data. We note that kinetic models of the form **1** → **9** + **11**, **1** → **6** → **9** + **11**, and models of the same form where the reactions are in equilibrium do not adequately fit the experimental data. Only a model wherein we consider an explicit dissociation and a direct path from **1** to **9** and **11** yielded reasonable fits to the kinetic data.

The experimental results shown in Figure 8 suggest that the rate constant for the direct conversion of **1** to **9** and **11** is only slightly higher than that of the pathway wherein **6** is able to dissociate from the catalyst. Given the similarity in the rate constants here, the flux through each pathway will likely be similar. To compare the experimentally measured activation barriers to the barriers computed from DFT, we used the Eyring equation. Using k_1 or k_2 yields $\Delta G^{\ddagger}$ = 30.34 ± 0.04 or 30.58 ± 0.06 kcal/mol, respectively. This activation barrier measured experimentally is within less than 3 kcal/mol of the computed free energy of activation (33.1 kcal/mol) from the rate-limiting pathway, which is within the expected error of DFT calculations of 1−3 kcal/mol.

CONCLUSIONS

Using DFT calculations, we were able to elucidate a number of mechanistic, kinetic, and thermodynamic parameters for the hydrogenolysis of C−O bonds that are relevant to biomass deconstruction using a Ru-xantphos catalyst.[22] First, we determined that coordination of **1** to [**Ru**] in an axial fashion is kinetically preferable to that in an equatorial fashion ($\Delta G^{\ddagger}_{ax}$ = 24.4 kcal/mol, $\Delta G^{\ddagger}_{eq}$ = 31.0 kcal/mol). In addition, we were able to determine that interconversion between a C- and O-bound enolate structure is thermodynamically accessible; while the C-bound enolate is thermodynamically more stable, the O-bound enolate is required for the reaction to proceed to completion. Furthermore, we concluded that the C−O bond cleavage step proceeds via an oxidative C−O bond addition and not the related oxidative C−H bond addition, since the former is kinetically favored over the latter ($\Delta G^{\ddagger}_{C-O}$ = 29.6 kcal/mol, $\Delta G^{\ddagger}_{C-H}$ = 43.1 kcal/mol). Related to the aforementioned, we were able to locate a transition structure for the C−O bond cleavage of **1** that includes an unprecedented 5-membered metallacycle, in contrast to an anticipated 3- or 4-membered transition structure. Finally, we were able to ascertain a preference for the release of phenol (**9**) before acetophenone (**11**) in the catalytic cycle: while there is little kinetic preference for the release of either phenol or acetophenone first, the ensuing step is much more facile for release of acetophenone than for phenol ($\Delta G^{\ddagger}_{11}$ = 22.5 kcal/mol, $\Delta G^{\ddagger}_{9}$ = 35.1 kcal/mol).

Along with a thorough DFT study, we experimentally determined the rate constants of this reaction by monitoring the concentration of all of the reactants and products using GC/MS. This allowed us to fit our experimental data based on the reaction steps and determine the rate constants for those steps. We were also able to compare the rate constant (and subsequent free energy of activation) of the first (first-order) step, namely, the catalytic acceptorless dehydrogenation of our substrate alcohol to the corresponding ketone. The experimentally determined free energy of activation (30.3 kcal/mol) compares favorably with that determined by DFT calculations (33.1 kcal/mol).

ASSOCIATED CONTENT

Ⓢ Supporting Information

Additional details of computational and experimental methods and fractional coordinates for all calculations. This material is available free of charge via the Internet at http://pubs.acs.org.

AUTHOR INFORMATION

Corresponding Author
*E-mail: robert.paton@chem.ox.ac.uk (R.S.P.), gregg.beckham@nrel.gov (G.T.B.).

Author Contributions
#These authors contributed equally to this paper.

Notes
The authors declare no competing financial interest.

ACKNOWLEDGMENTS

REFERENCES

(1) Bruneau, C.; Dérien, S.; Dixneuf, P. H. *Topics in Organometallic Chemistry*; Müller, T. J. J., Ed.; Springer-Verlag: Berlin, Germany, 2006; Vol. 19, pp 295−326.

(2) Grushin, V. V.; Alper, H. *J. Org. Chem.* **1991**, *56*, 5159−5161.

(3) Slatford, P. A.; Whittlesey, M. K.; Williams, J. M. J. *Tetrahedron Lett.* **2006**, *47*, 6787−6789.

(4) Ledger, A. E. W.; Slatford, P. A.; Lowe, J. P.; Mahon, M. F.; Whittlesey, M. K.; Williams, J. M. J. *Dalton Trans.* **2009**, *0*, 716−722.

(5) Hamid, M. H. S. A.; Slatford, P. A.; Williams, J. M. J. *Adv. Synth. Catal.* **2007**, *349*, 1555−1575.

(6) Kranenburg, M.; van der Burgt, Y. E. M.; Kamer, P. C. J.; van Leeuwen, P. W. N. M.; Goubitz, K.; Fraanje, J. *Organometallics* **1995**, *14*, 3081−3089.

(7) van Leeuwen, P. W. N. M.; Kamer, P. C. J.; Reek, J. N. H.; Dierkes, P. *Chem. Rev.* **2000**, *100*, 2741−2770.

(8) Freixa, Z.; van Leeuwen, P. W. N. M. *Dalton Trans.* **2003**, *0*, 1890−1901.

(9) Birkholz née Gensow, M.-N.; Freixa, Z.; van Leeuwen, P. W. N. M. *Chem. Soc. Rev.* **2009**, *38*, 1099−1118.

(10) Anand, N.; Owston, N. A.; Parker, A. J.; Slatford, P. A.; Williams, J. M. J. *Tetrahedron Lett.* **2007**, *48*, 7761−7763.

(11) Blacker, A. J.; Farah, M. M.; Hall, M. I.; Marsden, S. P.; Saidi, O.; Williams, J. M. J. *Org. Lett.* **2009**, *11*, 2039−2042.

(12) Watson, A. J. A.; Maxwell, A. C.; Williams, J. M. J. *Org. Biomol. Chem.* **2012**, *10*, 240−243.

(13) Takahashi, K.; Yamashita, M.; Tanaka, Y.; Nozaki, K. *Angew. Chem., Int. Ed.* **2012**, *51*, 4383−4387.

(14) Pridmore, S. J.; Slatford, P. A.; Williams, J. M. J. *Tetrahedron Lett.* **2007**, *48*, 5111−5114.

(15) Pridmore, S. J.; Slatford, P. A.; Taylor, J. E.; Whittlesey, M. K.; Williams, J. M. J. *Tetrahedron* **2009**, *65*, 8981−8986.

(16) Pridmore, S. J.; Slatford, P. A.; Daniel, A.; Whittlesey, M. K.; Williams, J. M. J. *Tetrahedron Lett.* **2007**, *48*, 5115−5120.

(17) Wise, N. J.; Williams, J. M. J. *Tetrahedron Lett.* **2007**, *48*, 3639−3641.

(18) Owston, N. A.; Parker, A. J.; Williams, J. M. J. *Chem. Commun. (Cambridge, U.K.)* **2008**, *0*, 624−625.

(19) Owston, N.; Nixon, T.; Parker, A.; Whittlesey, M.; Williams, J. *Synthesis* **2009**, *2009*, 1578−1581.

(20) Hall, M. I.; Pridmore, S. J.; Williams, J. M. J. *Adv. Synth. Catal.* **2008**, *350*, 1975−1978.

(21) Yu, D.-G.; Li, B.-J.; Shi, Z.-J. *Acc. Chem. Res.* **2010**, *43*, 1486−1495.

(22) Nichols, J. M.; Bishop, L. M.; Bergman, R. G.; Ellman, J. A. *J. Am. Chem. Soc.* **2010**, *132*, 12554−12555.

(23) Wu, A.; Patrick, B. O.; Chung, E.; James, B. R. *Dalton Trans.* **2012**, *41*, 11093−11106.

(24) vom Stein, T.; Weigand, T.; Merkens, C.; Klankermayer, J.; Leitner, W. *ChemCatChem* **2012**, *5*, 439−441.

(25) Bozell, J. J.; Holladay, J. E.; Johnson, D.; White, J. F. Top Value-Added Chemicals for Biomass. In *Energy*; U.S. D.O.E.: Washington, DC, 2007; Vol. *II*.

(26) Chundawat, S. P. S.; Beckham, G. T.; Himmel, M. E.; Dale, B. E. *Annu. Rev. Chem. Biomol. Eng.* **2011**, *2*, 121−145.

(27) Hicks, J. C. *J. Phys. Chem. Lett.* **2011**, *2*, 2280−2287.

(28) Rinaldi, R.; Schüth, F. *Energy Environ. Sci.* **2009**, *2*, 610−626.

(29) Son, S.; Toste, F. D. *Angew. Chem., Int. Ed.* **2010**, *49*, 3791−3794.

(30) Hanson, S. K.; Baker, R. T.; Gordon, J. C.; Scott, B. L.; Thorn, D. L. *Inorg. Chem.* **2010**, *49*, 5611−5618.

(31) Hanson, S.; Wu, R.; Silks, L. *Angew. Chem., Int. Ed.* **2012**, *51*, 3410−3413.

(32) Bozell, J. J.; Hames, B. R.; Dimmel, D. R. *J. Org. Chem.* **1995**, *60*, 2398−2404.

(33) Elder, T.; Bozell, J. J. *Holzforschung* **1996**, *50*, 24−30.

(34) Cedeno, D.; Bozell, J. J. *Tetrahedron Lett.* **2012**, *53*, 2380−2383.

(35) Desnoyer, A. N.; Fartel, B.; MacLeod, K. C.; Patrick, B. O.; Smith, K. M. *Organometallics* **2012**, *31*, 7625−7628.

(36) Sergeev, A. G.; Hartwig, J. F. *Science* **2011**, *332*, 439−443.

(37) Kelley, P.; Lin, S.; Edouard, G.; Day, M. W.; Agapie, T. *J. Am. Chem. Soc.* **2012**, *134*, 5480−5483.

(38) Frisch, M. J.; Trucks, G. W.; Schlegel, H. B.; Scuseria, G. E.; Robb, M. A.; Cheeseman, J. R.; Scalmani, G.; Barone, V.; Mennucci, B.; Petersson, G. A.; Nakatsuji, H.; Caricato, M.; Li, X.; Hratchian, H. P.; Izmaylov, A. F.; Bloino, J.; Zheng, G.; Sonnenberg, J. L.; Hada, M.; Ehara, M.; Toyota, K.; Fukuda, R.; Hasegawa, J.; Ishida, M.; Nakajima, T.; Honda, Y.; Kitao, O.; Nakai, H.; Vreven, T.; Montgomery, J. A.; , Jr., Peralta, J. E.; Ogliaro, F.; Bearpark, M.; Heyd, J. J.; Brothers, E.; Kudin, K. N.; Staroverov, V. N.; Kobayashi, R.; Normand, J.; Raghavachari, K.; Rendell, A.; Burant, J. C.; Iyengar, S. S.; Tomasi, J.; Cossi, M.; Rega, N.; Millam, J. M.; Klene, M.; Knox, J. E.; Cross, J. B.; Bakken, V.; Adamo, C.; Jaramillo, J.; Gomperts, R.; Stratmann, R. E.; Yazyev, O.; Austin, A. J.; Cammi, R.; Pomelli, C.; Ochterski, J. W.; Martin, R. L.; Morokuma, K.; Zakrzewski, V. G.; Voth, G. A.; Salvador, P.; Dannenberg, J. J.; Dapprich, S.; Daniels, A. D.; Ö. Farkas, Foresman, J. B.; Ortiz, J. V.; Cioslowski, J.; Fox, D. J. *Gaussian 09*, Rev. B.01; Gaussian, Inc.: Wallingford, CT, 2009.

(39) Zhao, Y.; Truhlar, D. G. *Acc. Chem. Res.* **2008**, *41*, 157−167.

(40) Pieniazek, S. N.; Houk, K. N. *Angew. Chem., Int. Ed.* **2006**, *45*, 1442−1445.

(41) Pieniazek, S. N.; Clemente, F. R.; Houk, K. N. *Angew. Chem., Int. Ed.* **2008**, *47*, 7746−7749.

(42) Paton, R. S.; Mackey, J. L.; Kim, W. H.; Lee, J. H.; Danishefsky, S. J.; Houk, K. N. *J. Am. Chem. Soc.* **2010**, *132*, 9335−9340.

(43) Paton, R. S.; Kim, S.; Ross, A. G.; Danishefsky, S. J.; Houk, K. N. *Angew. Chem., Int. Ed.* **2011**, *50*, 10366−10368.

(44) Paton, R. S.; Steinhardt, S. E.; Vanderwal, C. D.; Houk, K. N. *J. Am. Chem. Soc.* **2011**, *133*, 3895−3905.

(45) Wheeler, S. E.; Moran, A.; Pieniazek, S. N.; Houk, K. N. *J. Phys. Chem. A* **2009**, *113*, 10376−10384.

(46) Zhao, Y.; Truhlar, D. G. *J. Chem. Theory Comput.* **2009**, *5*, 324−333.

(47) Wadt, W. R.; Hay, P. J. *J. Chem. Phys.* **1985**, *82*, 284−298.

(48) Roy, L. E.; Hay, P. J.; Martin, R. L. *J. Chem. Theory Comput.* **2008**, *4*, 1029−1031.

(49) Fukui, K. *J. Phys. Chem.* **1970**, *74*, 4161−4163.

(50) Fukui, K. *Acc. Chem. Res.* **1981**, *14*, 363−368.

(51) Gonzalez, C.; Schlegel, H. B. *J. Phys. Chem.* **1990**, *94*, 5523−5527.

(52) Gonzalez, C.; Schlegel, H. B. *J. Chem. Phys.* **1989**, *90*, 2154−2162.

(53) Ishida, K.; Morokuma, K.; Komornicki, A. *J. Chem. Phys.* **1977**, *66*, 2153−2157.

(54) Legault, C. Y. *CYLview*, 1.0b; Université de Sherbrooke: Québec, Canada, 2009 (http://www.cylview.org)

(55) Barone, V.; Cossi, M. *J. Phys. Chem. A* **1998**, *102*, 1995−2001.

(56) Cossi, M.; Rega, N.; Scalmani, G.; Barone, V. *J. Comput. Chem.* **2003**, *24*, 669−681.

(57) Atwood, J. D. *Inorganic and Organometallic Reaction Mechanisms*, 2nd ed.; Wiley-VCH: New York, 1996.

(58) Orpen, A. G.; Connelly, N. G. *Organometallics* **1990**, *9*, 1206−1210.

(59) Lunder, D. M.; Lobkovsky, E. B.; Streib, W. E.; Caulton, K. G. *J. Am. Chem. Soc.* **1991**, *113*, 1837−1838.

(60) Poulton, J. T.; Folting, K.; Streib, W. E.; Caulton, K. G. *Inorg. Chem.* **1992**, *31*, 3190−3191.

(61) Poulton, J. T.; Sigalas, M. P.; Eisenstein, O.; Caulton, K. G. *Inorg. Chem.* **1993**, *32*, 5490−5501.

(62) Poulton, J. T.; Sigalas, M. P.; Folting, K.; Streib, W. E.; Eisenstein, O.; Caulton, K. G. *Inorg. Chem.* **1994**, *33*, 1476−1485.

(63) Yandulov, D. V.; Caulton, K. G.; Belkova, N. V.; Shubina, E. S.; Epstein, L. M.; Khoroshun, D. V.; Musaev, D. G.; Morokuma, K. *J. Am. Chem. Soc.* **1998**, *120*, 12553−12563.

(64) Kubas, G. J. *Catal. Lett.* **2005**, *104*, 79−101.

(65) Van der Sluys, L. S.; Kubas, G. J.; Caulton, K. G. *Organometallics* **1991**, *10*, 1033−1038.

(66) Dobereiner, G. E.; Crabtree, R. H. *Chem. Rev.* **2010**, *110*, 681−703.

(67) Besora, M.; Gourlaouen, C.; Yates, B.; Maseras, F. *Dalton Trans.* **2011**, *40*, 11089−11094.

(68) Hartwig, J. F.; Bergman, R. G.; Andersen, R. A. *J. Am. Chem. Soc.* **1990**, *112*, 3234−3236.

(69) Hartwig, J. F.; Bergman, R. G.; Andersen, R. A. *Organometallics* **1991**, *10*, 3326−3344.

(70) Bartoszewicz, A.; Jeżowska, M. M.; Laymand, K.; Möbus, J.; Martín-Matute, B. *Eur. J. Inorg. Chem.* **2012**, *2012*, 1517−1530.

(71) Ueno, S.; Mizushima, E.; Chatani, N.; Kakiuchi, F. *J. Am. Chem. Soc.* **2006**, *128*, 16516−16517.

(72) Matsubara, T.; Koga, N.; Musaev, D. G.; Morokuma, K. *Organometallics* **2000**, *19*, 2318−2329.

(73) Kakiuchi, F.; Usui, M.; Ueno, S.; Chatani, N.; Murai, S. *J. Am. Chem. Soc.* **2004**, *126*, 2706−2707.

(74) Kim, S.; Chmely, S. C.; Nimlos, M. R.; Bomble, Y. J.; Foust, T. D.; Paton, R. S.; Beckham, G. T. *J. Phys. Chem. Lett.* **2011**, *2*, 2846−2852.

(75) Murdoch, J. R. *J. Chem. Educ.* **1981**, *58*, 32−36.

(76) Kozuch, S.; Shaik, S. *Acc. Chem. Res.* **2011**, *44*, 101−110.

(77) The most plausible mechanism for the interconversion of the axial and equatorial forms is via a dissociation and reassociation, in which the ketone and catalyst separate and recombine in a different orientation. While there would be transition states on the free energy surface, on the potential energy surface (PES), the energy change is unlikely to show any saddle points for this process, since this is essentially dative bond cleavage/formation.

(78) Seeman, J. I. *Chem. Rev.* **1983**, *83*, 83−134.

(79) Hoops, S.; Sahle, S.; Gauges, R.; Lee, C.; Pahle, J.; Simus, N.; Singhal, M.; Xu, L.; Mendes, P.; Kummer, U. *Bioinformatics* **2006**, *22*, 3067−3074.